Desalination and Water Treatment
www.deswater.com

doi: 10.5004/dwt.2018.22421

118 (2018) 314–325
June

High-capacity adsorption of cationic dyes using porous magnetic adsorbent

Taotao Lu[a,b,c], Yongfeng Zhu[a], Yanxing Qi[a,c,*], Wenbo Wang[a], Aiqin Wang[a,*]

[a]*Key Laboratory of Clay Mineral Applied Research of Gansu Province, Center of Eco-material and Green Chemistry, Lanzhou Institute of Chemical Physics, Chinese Academy of Sciences, Lanzhou 730000, China, Tel. +86 931 4968118; Fax: +86 931 8277088; emails: aqwang@licp.cas.cn (A. Wang), qiyx@licp.cas.cn (Y. Qi), lzltt_2009@163.com (T. Lu), zhuyf851013@163.com (Y. Zhu), wbwang@licp.cas.cn (W. Wang)*
[b]*University of Chinese Academy of Sciences, Beijing 100049, China*
[c]*National Engineering Research Center for Fine Petrochemical Intermediates, Lanzhou Institute of Chemical Physics, Chinese Academy of Sciences, Lanzhou 730000, China*

Received 21 October 2017; Accepted 22 April 2018

ABSTRACT

A novel porous magnetic adsorbent with sufficient interconnected pore structure of chitosan-*g*-poly(2-acrylamide-2-methylpropane sulfonic acid) (CTS-*g*-AMPS) was prepared by grafting AMPS onto CTS via Pickering high internal phase emulsions (Pickering-HIPEs) polymerization, which stabilized with the modified Fe_3O_4 nanoparticles, and used for the removal of the cationic dyes methylene blue (MB), brilliant green (BG), and methyl green (MG) from aqueous solution. The effects of initial pH, contact time, and initial concentration on the adsorption properties of the porous adsorbent were studied systematically. It was revealed that the porous magnetic adsorbent can rapidly adsorb MB, BG, and MG with high adsorption capacities within a wide pH range from 6.0 to 12.0. The maximum adsorption capacities can be reached to 1,044.56, 1,625.94, and 908.01 mg/g for MB, BG, and MG, respectively, within 20 min. After adsorption of MB, BG, and MG, the porous magnetic adsorbent can be recycled easily from the solution by a magnet, and regenerated for reuse. The adsorption capacities of the adsorbent still reached 1,010.02, 1,578.73, and 889.01 mg/g for MB, BG, and MG, respectively, after five adsorption–desorption cycles. The recyclable magnetic adsorbent showed high adsorption capacity, fast adsorption rate, and excellent reusability, and can be used as a potential adsorbent for the decontamination of dye-polluted water.

Keywords: Magnetic; Porous adsorbent; Pickering-HIPEs; Adsorption; Cationic dyes

1. Introduction

Dyes have been extensively used in many industrial areas such as cosmetic, leather, printing, paper, food, textile, and others. It has been reported that about 7×10^5 tons and 10,000 types of dyes have been produced annually over the world, and approximately 10%–15% of the dyes were released into the environment [1–3], which caused serious harm to aquatic organism and human health because these dyes are toxic and non-biodegradable [4–7]. Over the years, great progress has been made in the removal of dye contaminants in water, and especially various adsorbent materials such as activated carbon [8], graphene oxide/chitin nanofibril composite foams [9], silica–polymer hybrid materials [10], metal–organic framework composite [11], hydrogels [12], and porous materials [13,14] have been developed and used successively. Among them, activated carbon is the most widely used adsorbent for organic pollutants due to its rich pores and excellent adsorption performance [15,16]. However, the practical applications of activated carbon remain limited because it can only adsorb organic matters by physical pore adsorption, and so the adsorption capacity and rate are limited, and further regeneration is difficult [17]. As a consequence, it still remains a challenge to design and develop

* Corresponding author.

high-efficient adsorbent with high adsorption capacity, fast adsorption rate, and better regeneration performance.

Recently, porous polymer adsorbents have gained increasing attention due to their high porosity, tunable pore size, interconnected pore structure, and sufficient functional groups [18–20]. Especially, the porous adsorbents from the particle-stabilized Pickering high internal phase emulsions (Pickering-HIPEs) have lower toxicity, tailored functional groups, ease of operation, and control advantages [21–23]. Moreover, the stabilized particles can not only stabilize the HIPEs by irreversibly anchoring on droplet surfaces, but also initiate polymerization, crosslink the polymer, and/or functionalize the void surfaces [24,25]. For example, Liu et al. [11] synthesized polymer microspheres stabilized by titania nanoparticles from Pickering emulsion template, which can form continuous films with potential applications for photo-catalyst, water and air purification. And Mert et al. [26] prepared the magnetic poly-HIPEs based on styrene-*co*-divinylbenzene with open cellular architecture of large pores and interconnected small pores and it was easy for separation from the solution. Even if the porous materials prepared from Pickering-HIPEs template has been used in the oil–water separation, CO_2 adsorption, heavy metal removal, and so on, but the related study in the dye removal is rare.

In order to get the new adsorbents with excellent adsorptive property such as high adsorption capacity, fast adsorption rate, and good recyclability for treatment of dyes, a series of the magnetic porous adsorbents of chitosan-*g*-poly(2-acrylamide-2-methylpropane sulfonic acid) (CTS-*g*-AMPS) were prepared by the polymerization reaction from Pickering-HIPEs stabilized with modified Fe_3O_4 and then used for removal of three typical dyes of methylene blue (MB), brilliant green (BG), and methyl green (MG) in aqueous solution. The effects of adsorption parameters including pH, initial concentration, and contact time on the adsorption properties, as well as the reusable performance of the adsorbent were investigated systematically.

2. Experimental

2.1. Materials

2-Acrylamide-2-methylpropane sulfonic acid (AMPS, C.R. grade) was purchased from Adamas Reagent Co., Ltd. (Beijing, China). Chitosan (CTS, the degree of deacetylation is 0.85, and the average molecular weight is 600 kDa) was purchased from Zhejiang Yuhuan Ocean Biology Co., Ltd. (Zhejiang, China). Pluronic F68 (B.R. grade) was obtained from Wuhan Kangbaotai Fine-Chemical Co., Ltd. (Wuhan, China). *N, N′*-methylenebisacrylamide (MBA, C.R. grade), ammonium persulfate (APS, A.R. grade), *N, N, N, N*-tetramethyl ethylenediamine (TMEDA, A.R. grade), $FeCl_3{\cdot}6H_2O$ (A.R. grade), sodium citrate (A.R. grade), sodium acetate (A.R. grade), P-xylene (PX, A.R. grade), and ethyl alcohol (A.R. grade) were purchased from Kemiou Chemical Reagent Co., Ltd. (Tianjin, China). The silicone of tetraethyl orthosilicate (TEOS, C.P. grade) and 3-aminopropyltrimethoxysilane (APTMS, C.P. grade) were purchased from Union Silicon Chemical Co., Ltd. (Nanjing, China). MB, BG and MG were all analytical grade and all solutions were prepared with deionized water.

2.2. Preparation of the CTS-*g*-AMPS porous magnetic adsorbents

The CTS-*g*-AMPS porous magnetic adsorbents were prepared from O/W Pickering-HIPEs stabilized with the modified Fe_3O_4 nanoparticles (denoted as Fe_3O_4-MNPs-M) by the method of our group reported previously [27]. 0.1 g CTS, 0.72 g MBA, 4.14 g AMPS and an appropriate amount of Fe_3O_4-MNPs-M and cosurfactant Pluronic F68 were added into a three-neck round-bottomed flask equipped with a mechanical stirrer, and the mixtures were stirred at 700 rpm for 1 h. Subsequently, PX was added into the aqueous phase dropwise and stirred at 900 rpm for another 2 h. After that, 0.15 g of APS and 50 μL of TMEDA were added under the moderate agitation and the resultant Pickering-HIPEs was transferred into the mold tubes and cured at 45°C for 4 h. The resulting bulk polymers were washed with alcohol via Soxhlet extraction and then immersed in the solution of NaOH in water/alcohol mixture ($V_{water}/V_{ethanol}$ = 3/7) for 24 h. The final products were subsequently dried in an oven at 40°C for 24 h. The detailed information about the feeding compositions is summarized in Table S1.

2.3. Batch adsorption studies

The adsorption performance of the porous magnetic adsorbents for three cationic dyes (MB, BG, and MG) was evaluated by the following procedure. Typically, 25 mg of the adsorbent was added to 25 mL of dye solutions, and the resultant mixtures were shaken in a thermostatic orbital shaker (THZ-98A) at 30°C and 150 rpm for a given time. After the adsorption, the adsorbent was separated by a magnet and the concentration of cationic dyes in the solution was analyzed using a UV–vis spectrophotometer (TU-1900) (the maximum absorption wavelengths are 665, 624, and 630 nm for MB, BG, and MG, respectively). The equilibrium adsorption capacity (q_e, mg/g) for cationic dyes was calculated according to Eq. (1) as follows:

$$q_e = \frac{(C_0 - C_e)V}{m} \tag{1}$$

where q_e is the adsorption capacity (mg/g), C_0 and C_e are the initial and equilibrium concentrations of cationic dyes (mg/L), V is the volume of solution of cationic dyes (mL), and m is the mass of adsorbent used (mg).

In order to prove the porous adsorbent has high adsorption capacity and fast adsorption rate, herein, the adsorption kinetics was studied by varying the contact time from 0 to 120 min, and the pseudo-first-order and pseudo-second-order equations were used to analyze the dynamic adsorption process. The adsorption isotherms were studied by increasing the initial dye concentrations from 100 to 2,000 mg/L, and the Langmuir and Freundlich isotherm models were used to fit the experimental data and analyze the thermodynamic adsorption process. The influence of pH on the adsorption of MB, BG, and MG was studied in the pH ranges of 1.0–12.0. The cationic dye solutions at pH = 1.0 or pH = 12.0 were prepared by using the 0.5 mol/L of HCl or NaOH, and the other pH values of solutions were adjusted with 0.1 mol/L HCl or NaOH solutions. The reusability of the adsorbent was studied by evaluating the adsorption capacity of the adsorbent

after regenerating by adsorption–desorption process for five cycles. In this process, the dye-loaded adsorbent was immersed in 25 mL of 0.1 mol/L HCl solution for 4 h, and then activated by soaking in 25 mL of 0.1 mol/L NaOH solution for 30 min. The regenerated adsorbent was washed fully with deionized water and then used for the next adsorption cycles. To assure the accuracy of data, all adsorption experiments were carried out for three times under the same conditions, and the averages of three experiments were reported with the standard deviation less than 5%.

2.4. Characterizations

The surface morphology was observed on a Field Emission Scanning Electron Microscope (JSM-6701F, JEOL, Japan). The magnetic porous adsorbents before and after adsorption were characterized by the fourier transform infrared (FTIR) spectra recorded on the Nicolet NEXUS FTIR spectrometer (USA) in the wavenumber range of 4,000–400 cm^{-1}. Magnetic properties of the magnetic porous adsorbents were detected by a vibrating sample magnetometer (VSM, Lakeshore 7304). The morphologies of the Fe_3O_4 and Fe_3O_4-MNPs-M were characterized with a JEM-1200EX/S transmission electron microscopy (TEM, JEOL, Tokyo, Japan). The X-ray diffraction (XRD) analysis of Fe_3O_4-MNPs-M was obtained using an X'Pert PRO diffractometer (X'Pert PRO, PAN analytical Co., Netherlands) equipped with a Cu-Kα radiation source from 3° to 80° (2θ). The zeta potentials of adsorbent were measured on a Malvern Zetasizer Nano system with irradiation from a 633 nm He-Ne laser (Malvern Zeta voltmeter, ZEN3600, Britain). The pore size distribution was estimated by counting 200 pores using Image-Pro Plus as a software tool providing the number distribution of pores.

3. Results and discussion

3.1. The magnetic porous adsorbent

The diameter of regular spherical Fe_3O_4-MNPs was about 110 nm, and increased to about 150 nm after modification with organosilane (Fig. S1). The characterization results of FTIR (Fig. S2) and XRD (Fig. S1) analysis confirmed that the Fe_3O_4-MNPs-M was successfully prepared by coating the organosilane on Fe_3O_4-MNPs. After the polymerization reaction, the FTIR spectra of CTS-*g*-AMPS (Fig. S3) showed that the characteristic bands assigning to $–NH_2$ (1,655 and 1,589 cm^{-1}) and –OH (3,420 cm^{-1}) of CTS decreased or even disappeared [28], and the characteristic absorption bands, attributing to the asymmetric stretching vibration of two –S=O and S–O– [29], were appeared at 1,191, 1,045 and 629 cm^{-1}. These results indicated that the NH_2 and OH of CTS had taken part in the polymerization reaction and the CTS-*g*-AMPS adsorbent was successfully prepared. In addition, Fe and Si-element derived from Fe_3O_4-MNPs-M were uniformly distributed in the element mapping images and energy dispersive X-ray spectroscopy (EDX) curve of the porous adsorbent (Fig. S4), which suggested that the Fe_3O_4-MNPs-M was involved in stabilizing the oil droplets and distributed homogeneously at the interface acting as a barrier against oil droplet coalescence, and finally they fixed within the network of the porous adsorbent after the polymerization reaction. We prepared a series of porous adsorbent by varying the volume of the disperse phase, the amount of the cosurfactant and Fe_3O_4-MNPs-M. All of the samples had sufficient interconnected pore structure (Fig. S5) and the CTS-*g*-AMPS-2 had the narrowest pore size distribution (Fig. 1). The average pore size and the windows size of the CTS-*g*-AMPS-2 were 4.19 and 0.62 μm, respectively. The specific surface area was calculated with the total drop surface area of the magnetic porous adsorbent according to the equation as follows [30]:

$$S_d = 4\pi R^2 \times \frac{3V_{oil}}{4\pi R^3} = \frac{3V_{oil}}{R} \quad (2)$$

where V_{oil} is the volume of oil included in the emulsion and R is the Sauter mean radius of the droplets by estimation. According to the equation, the CTS-*g*-AMPS-2 has the larger total drop surface area (S_d) of about 17.18 m^2. The results of VSM (Fig. S6) of Fe_3O_4-MNPs, Fe_3O_4-MNPs-M, and the magnetic porous adsorbent showed that the saturation magnetizations were about 60.48, 33.07 and 0.74 emu/g, respectively, and no reduced remanence and coercivity being zero were detected, indicating that they were superparamagnetic with negligible remanence of magnetization. Although the magnetic porous adsorbent had a weaker magnetism, it also can be separated easily from the adsorbed solution.

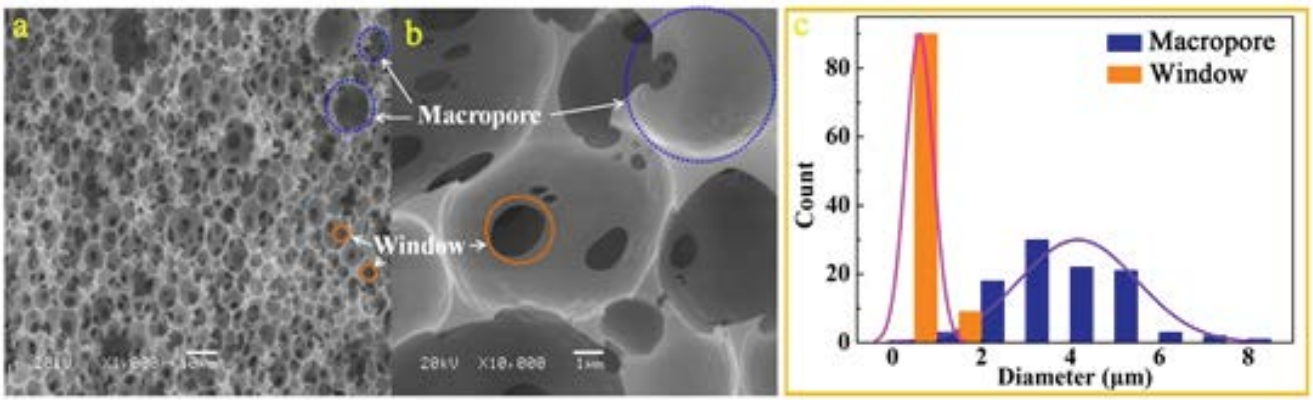

Fig. 1. SEM images (a) and (b), and the pore size distribution (c) of the CTS-*g*-AMPS-2 magnetic porous adsorbent.

3.2. Effect of pH on cationic dyes adsorption

The porous adsorbent of CTS-*g*-AMPS-2 with narrowest pore size distribution and the maximal total drop surface area was used in the adsorption of dyes. And the adsorption experiments were carried out at different pH values from 1.0 to 12.0 to study the effects of pH on the adsorption capacity. As shown in Fig. 2, the adsorption capacities of the CTS-*g*-AMPS-2 adsorbent for MB, BG, and MG dyes exhibit similar change trend with altering the pH from 1.0 to 12.0. The adsorption capacity obviously increased with increasing the pH from 1.0 to 6.0 and remained a constant in the range of 6.0–12.0. Because of the sulfonic group can completely deprotonate in the solution, the increased adsorption capacity in the range of 1.0–6.0 was due to the deprotonation reaction of the imine originated from the AMPS and the competitive adsorption between the H^+ and MB, BG, and MG. The deprotonation process of the imine can be proven by the more and more negative of zeta potentials in the pH of 1.0–8.0 (Fig. S7). When all the imine were deprotonated, the saturation adsorption has reached. The competitive adsorption behavior between the H^+ and MB, BG, and MG was stronger in the lower pH value. When the pH increased upon 6.0, the competitive adsorption disappeared, and the corresponding adsorption capacity reached the flatform. It is worth noticing that the adsorbent shows high adsorption capacity in a wide pH range, indicating that the adsorbent can be applied in a wide pH range as a promising adsorbent material for removal of cationic dyes.

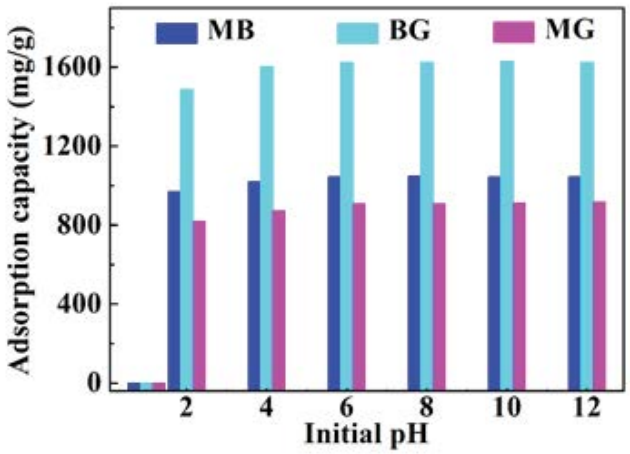

Fig. 2. Effect of pH on the adsorption of CTS-*g*-AMPS-2 for MB, BG, and MG. Adsorption conditions: C_0: MB: 1,200 mg/L, BG: 1,800 mg/L, and MG: 1,000 mg/L; pH range: 1.0–12.0; equilibrium time: 120 min; 25 mg/25 mL; temperature: 30°C.

3.3. Effect of contact time on cationic dyes adsorption

Fig. 3(a) shows the variation of adsorption capacity versus contact time. It can be seen that the adsorption capacities of CTS-*g*-AMPS-2 for MB, BG, and MG rapidly increased with increasing the contact time, and the adsorption equilibrium can be achieved rapidly within 20 min (for MB), 10 min (for BG), and 20 min (for MG), respectively.

In order to understand the dynamic adsorption process, the pseudo-first-order (Eq. (3)) [31] and the pseudo-second-order kinetic models (Eq. (4)) [32] were used to fit the adsorption data:

$$\log\left(q_e - q_t\right) = \log q_e - \left(\frac{k_1}{2.303}\right)t \tag{3}$$

$$\frac{t}{q_t} = \frac{1}{k_2 q_e^2} + \frac{t}{q_e} \tag{4}$$

where q_e and q_t are the amount of dyes adsorbed (mg/g) at equilibrium state and at time t, respectively. k_1 and k_2 are the rate constant calculated by fitting with pseudo-first-order and pseudo-second-order kinetic equations, respectively.

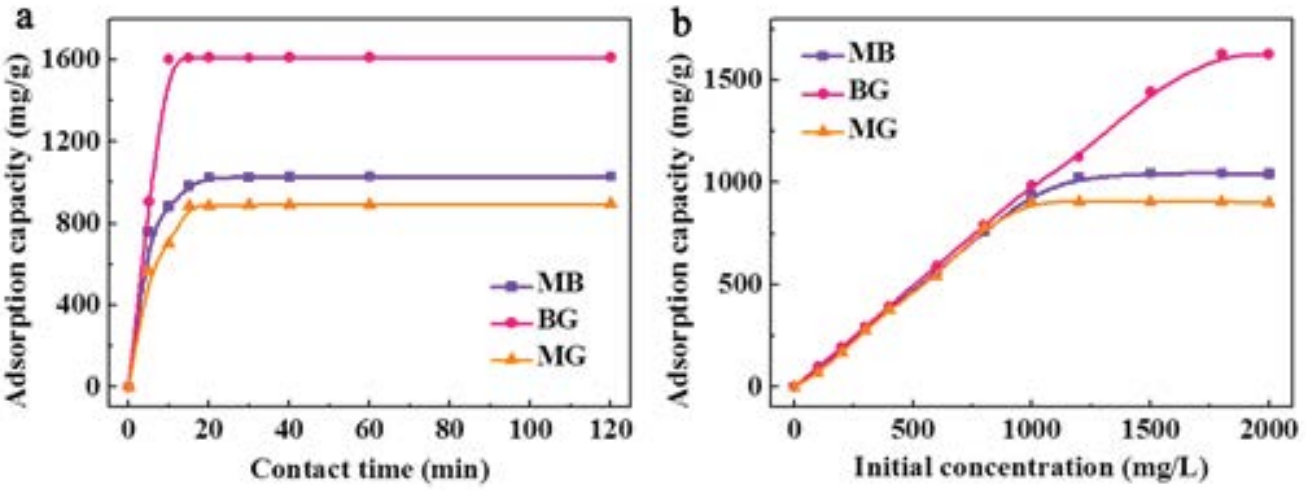

Fig. 3. Effect of contact time (a) and initial concentration (b) on the adsorption of MB, BG, and MG. Experimental conditions for adsorption kinetics: C_0: MB: 1,200 mg/L, BG: 1,800 mg/L, and MG: 1,000 mg/L; pH 6.0; equilibrium time: 120 min; experimental conditions for adsorption isotherms: 25 mg/25 mL; pH: 6.0; temperature: 30°C.

The estimated model parameters with the linear correlation coefficient (R^2) are listed in Table 1 and the corresponding curves are shown in Fig. 4. The higher R^2 values (>0.99) were obtained by fitting with pseudo-second-order kinetic model, and theoretical adsorption capacity was also close to the experimental value, indicating that the adsorption process can be described well by pseudo-second-order kinetic model, and the adsorption rate mainly contributed by the chemical interaction between the dye molecular and the adsorption sites.

3.4. Effect of initial concentration on cationic dyes adsorption

As shown in Fig. 3(b), the adsorption capacities increased with increasing the concentration of MB, BG, and MG solution until the adsorption saturation was reached. The higher concentration of MB, BG, and MG provided stronger driving force for adsorption, which was helpful to accelerating the diffusion of cationic dye molecules onto the surface of adsorbent, so that the adsorption capacity increased with

Table 1
Estimated adsorption kinetic parameters for MB, BG, and MG by pseudo-first-order and pseudo-second-order models

Adsorbate	C_0 (mg/L)	$q_{e,exp}$ (mg/g)	Pseudo-first-order model			Pseudo-second-order model		
			$q_{e,cal}$ (mg/g)	k_1 (min^{-1})	R^2	$q_{e,cal}$ (mg/g)	$k_2 \times 10^{-4}$ ((g/mg)/min)	R^2
MB	1,200	1,028.10	364.70	0.1367	0.8616	1,040.66	9.51	0.9996
BG	1,800	1,611.19	68.95	0.1169	0.6153	1,632.29	6.09	0.9986
MG	1,000	894.46	133.27	0.0913	0.6219	909.09	7.51	0.9990

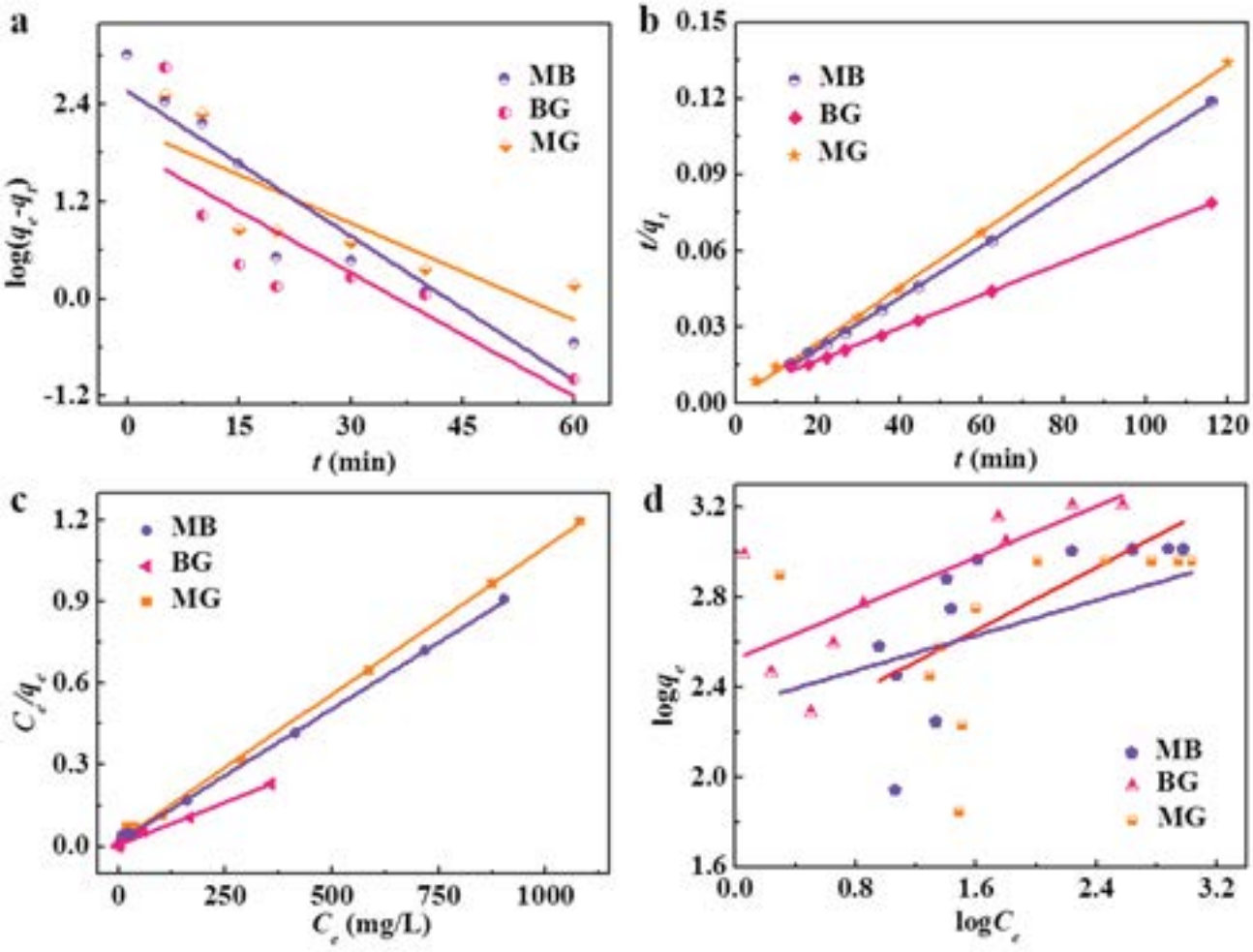

Fig. 4. Adsorption kinetic curves of MB, BG, and MG on CTS-*g*-AMPS-2 by pseudo-first-order kinetic model (a) and pseudo-second-order kinetic model (b); Langmuir adsorption isotherms (c) and Freundlich adsorption isotherms (d) of MB, BG, and MG on CTS-*g*-AMPS-2.

increasing the initial concentration. The maximum adsorption capacities of CTS-*g*-AMPS-2 reached 1,044.56 mg/g (3.26 mmol/g), 1,625.94 mg/g (3.36 mmol/g), and 908.01 mg/g (1.39 mmol/g) for MB, BG, and MG, respectively, which were higher than most of the other reported adsorbents (Table 2). It also can be seen that the porous adsorbent CTS-*g*-AMPS-2 showed both high adsorption capacities for MB, BG, and MG and stronger adsorption interactions with MB and BG. Due to the supermacroporous and interconnected structure, the porous adsorbent CTS-*g*-AMPS-2 can effectively remove the cationic dyes MB, BG, and MG, regardless of the size of the dye molecules. Although the structure of MG was similar to that of BG, the differences in adsorption were caused mainly by the positive charges of dye molecules. Namely, because MG owned two positive charges, it was needed more adsorption sites (SO_3^-) for adsorption the same amount of MG than that of MB and BG by electrostatic force [33,34]. Hence, when the adsorbent dosage was the same, the adsorption capacity of MG was lower than those of MB and BG.

Langmuir and Freundlich isotherm models are the commonly used models to study the adsorption isotherm, so that the adsorption data were fitted with Langmuir (Eq. (5)) [47] and Freundlich [48] (Eq. (6)) isotherm models to understand the adsorption process.

$$\frac{C_e}{q_e} = \frac{1}{q_m b} + \frac{C_e}{q_m} \tag{5}$$

$$\log\left(q_e\right) = \frac{1}{n}\log\left(C_e\right) + \log K \tag{6}$$

where C_e is the equilibrium concentration (mg/L), q_m and q_e are the adsorption capacities at equilibrium and at any time t (mg/g), respectively. b (L/mg) is the Langmuir constant related to the affinity of binding sites, K and n are the Freundlich constants related to the adsorption capacity and the adsorption intensity, respectively. The adsorption parameters calculated by fitting with the two isotherm equations are listed in Table 3 and the corresponding curves are shown in Fig. 4(c) and (d). The linear correlation coefficient ($R^2 > 0.994$) was obtained by fitting with Langmuir isotherm model, instead of Freundlich isotherm model, indicating that the adsorption data were well fitted with Langmuir isotherm and the cationic dyes were adsorbed onto the adsorbent surface with a monolayer coverage.

3.5. Regeneration and reusability

The recyclability of the adsorbent is very important for the practical application. In this study, the CTS-*g*-AMPS-2 adsorbent after adsorption of the cationic dyes (MB, BG, and MG) was desorbed with 0.1 mol/L HCl solution and then regenerated with 0.1 mol/L NaOH solution. After adsorption of MB, BG, and MG, the adsorbent can be separated conveniently from the solution by a magnet. Fig. 5 shows the effect of regeneration times of CTS-*g*-AMPS-2 on the adsorption efficiency. Obviously, the adsorption properties of CTS-*g*-AMPS-2 for MB, BG, and MG did not decrease obviously after five recycling tests, and the adsorption capacity of CTS-*g*-AMPS-2 for MB, BG, and MG still reached up to 1,010.02, 1,578.73, and 889.01 mg/g, respectively, revealing that the magnetic porous adsorbent had excellent recyclability.

3.6. Adsorption mechanism

The zeta potentials (Table S2) and the FTIR spectra changes of the porous adsorbents before and after adsorption

Table 2
Comparison of adsorption capacities (mg/g) of different adsorbents for MB, BG, and MG and the time required for reaching the adsorption equilibrium (min)

Adsorbents		Adsorbate	Adsorption capacity (mg/g)	Time (min)
Oak acorn peel [35]		MB	109.43	180
The wheat straw [36]		MB	205.40	50
Modified zeolite adsorbent [37]		MB	86.70	60
Mesoporous bioactive glasses [38]		MB	157.30	400
This study		MB	1,044.56	20
Polyurethane foam [39]		BG	134.95	200
Surfactant doped polyaniline/multiwalled carbon nanotubes (MWCNTs) composite [40]		BG	476.19	240
Cactus fruit peel [41]		BG	166.66	60
Mesoporous aluminosilicate [42]		BG	232.60	15
This study		BG	1,625.94	10
Waste tire activated carbon [43]		MG	29.23	80
Reduced graphene oxide [44]		MG	729.40	60
Pinus brutia cones [45]	Alkaline treatment	MG	214.00	60
	Acidic treatment		57.00	80
MWCNTs [46]		MG	119.05	100
This study		MG	908.01	20

Table 3
The constant parameters and correlation coefficients of Langmuir model and Freundlich model for MB, BG, and MG adsorption onto the adsorbent CTS-*g*-AMPS-2

Adsorbates	$q_{e,exp}$ (mg/g)	Langmuir model			Freundlich model		
		$q_{e,cal}$ (mg/g)	b (L/mg)	R^2	K	n	R^2
MB	1,044.56	1,065.04	0.0652	0.9993	124.8	2.85	0.4696
BG	1,625.94	1,660.45	0.1105	0.9941	334.7	3.51	0.5162
MG	908.01	925.92	0.0521	0.9984	205.2	5.12	0.1028

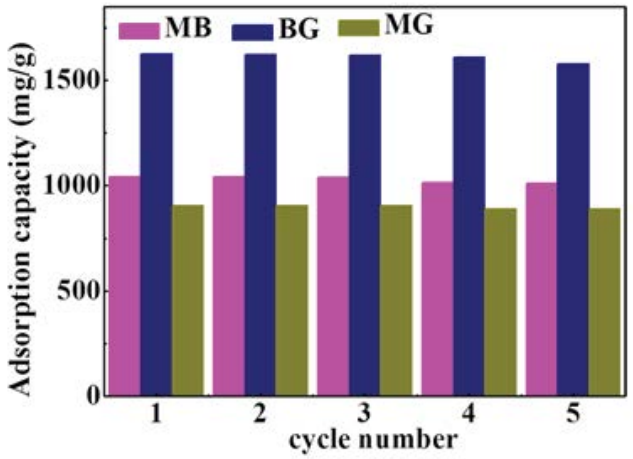

Fig. 5. The reusability of the as-prepared CTS-*g*-AMPS-2 for adsorption of MB, BG, and MG. Adsorption conditions: pH: 6.0; temperature: 30°C.

(Fig. 6) were discussed to investigate the adsorption mechanism. The porous adsorbents CTS-*g*-AMPS-2 showed a negative zeta potential with the average of −23.5 mV. However, the obvious changes of zeta potential occurred after adsorption of MB, BG, and MG, with reduction from an average of −23.5 to −1.26, −1.37, and −1.34 mV, respectively. Besides, the obvious bands shift also can be observed in the FTIR spectra. The absorption bands of CTS-*g*-AMPS-2 at 1,191, 1,045, and 629 cm^{-1} were assigned to the asymmetric stretching vibration of two –S=O and –S–O, respectively. After adsorption of MB, the new absorption bands appeared at 1,601, 1,395, and 1,340 cm^{-1}, which are ascribed to the stretching vibrations of the C=N (or C=C) groups, the C–N groups in the heterocycle, and the C–N groups connected to benzene ring (and N–CH_3), respectively. The overlapping of the stretching vibration bands of C=S at 1,177 cm^{-1}, C–S at 1,141 cm^{-1} between the peak of –S=O deformation vibration, causes the increase of the intensity of the final peak at 1,178 cm^{-1} [49]. After adsorption of BG, the new band at 1,582 cm^{-1} was assigned to the C=N bond contained in the quinoid structure of BG, which overlapped with the –N–H absorption band of CTS-*g*-AMPS-2. In addition, the two bands at 2,977 and 2,931 cm^{-1} were assigned to the asymmetric and symmetric vibrations of the aliphatic

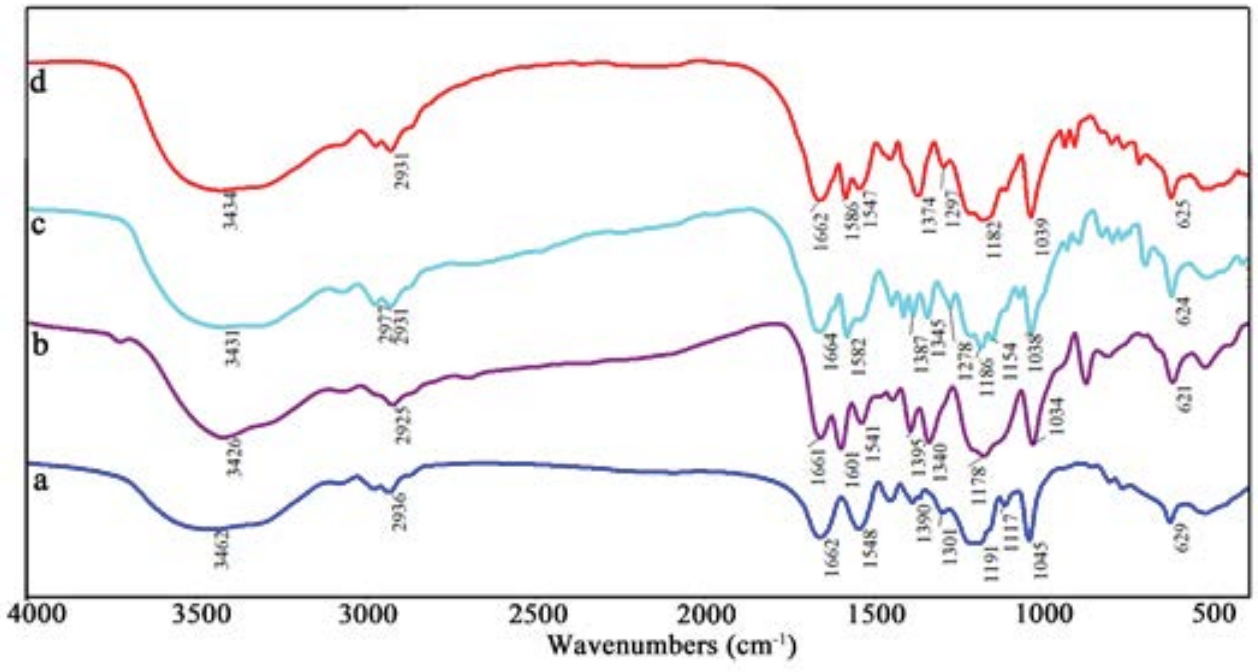

Fig. 6. FTIR spectra of CTS-*g*-AMPS-2 before (a) and after MB (b), BG (c) and MG (d) adsorption.

C–H bonds in CH_3 and CH_2 groups, which increased after the adsorption of BG [50]. While adsorbed MG, the bands at 1,586 cm^{-1} corresponding to $=N^+$ immonium ion appeared [44]. Moreover, after the adsorption of MB, BG, and MG, the absorption bands of CTS-*g*-AMPS-2 at 3,462 cm^{-1} (–OH or N–H groups), 1,191 and 1,045 cm^{-1} (–S=O groups), and 629 cm^{-1} (S–O– groups) shift to low wavenumbers region, respectively. All these changes revealed that the MB, BG, and MG molecules adsorbed onto the CTS-*g*-AMPS-2 through electrostatic attraction.

4. Conclusions

The open-cellular and recyclable CTS-*g*-AMPS porous magnetic adsorbents were successfully prepared by the in-situ polymerization from Pickering-HIPEs. The structure characterization results suggested the obtained porous magnetic adsorbent had sufficient interconnected pore structure, and abundant functional groups. The adsorption results showed that the porous magnetic adsorbent CTS-*g*-AMPS-2 had excellent adsorption property on cationic dyes of MB, BG, and MG, and the adsorption capacities for MB, BG, and MG reached up to 1,044.56, 1,625.94, and 908.01 mg/g, respectively, within a short time and in a wide pH range from 6.0 to 12.0. The five adsorption–desorption studies showed that the prepared adsorbent could be easily separated from polluted water and the adsorption capacity still reached 1,010.02, 1,578.73, and 889.01 mg/g for MB, BG, and MG, respectively. Consequently, this porous magnetic adsorbent has the potential to remove the cationic dyes from wastewater.

Acknowledgment

The authors thank the financial support of the National Natural Science Foundation of China (21377135, U1407114, and 51403221).

References

[1] S. Akhtar, A.A. Khan, Q. Husain, Potential of immobilized bitter gourd (*Momordica charantia*) peroxidases in the decolorization and removal of textile dyes from polluted wastewater and dyeing effluent, Chemosphere, 60 (2005) 291–301.
[2] M.D. Dey, R. Shukla, N.K. Bordoloi, R. Doley, R. Mukhopadhyay, Mechanism of adsorptive removal of methylene blue using dried biomass of *Rhizopus oryzae*, Appl. Biochem. Biotechnol., 177 (2015) 541–555.
[3] U. Pal, A. Sandoval, S.I.U. Madrid, G. Corro, V. Sharma, P. Mohanty, Mixed titanium, silicon, and aluminum oxide nanostructures as novel adsorbent for removal of rhodamine 6G and methylene blue as cationic dyes from aqueous solution, Chemosphere, 163 (2016) 142–152.
[4] S.M. Hussain Gardazi, T. Ashfaq Butt, N. Rashid, A. Pervez, Q. Mahmood, M. Maroof Shah, M. Bilal, Effective adsorption of cationic dye from aqueous solution using low-cost corncob in batch and column studies, Desal. Wat. Treat., 57 (2016) 28981–28998.
[5] H. Qiao, Y. Zhou, F. Yu, E. Wang, Y. Min, Q. Huang, L. Pang, T. Ma, Effective removal of cationic dyes using carboxylate-functionalized cellulose nanocrystals, Chemosphere, 141 (2015) 297–303.
[6] S. Agarwal, V.K. Gupta, M. Ghasemi, J. Azimi-Amin, *Peganum harmala*-L Seeds adsorbent for the rapid removal of noxious brilliant green dyes from aqueous phase, J. Mol. Liq., 231 (2017) 296–305.
[7] N. Hegyesi, R.T. Vad, B. Pukánszky, Determination of the specific surface area of layered silicates by methylene blue adsorption: the role of structure, pH and layer charge, Appl. Clay Sci., 146 (2017) 50–55.
[8] S. Hajati, M. Ghaedi, B. Barazesh, F. Karimi, R. Sahraei, A. Daneshfar, A. Asghari, Application of high order derivative spectrophotometry to resolve the spectra overlap between BG and MB for the simultaneous determination of them: ruthenium nanoparticle loaded activated carbon as adsorbent, J. Ind. Eng. Chem., 20 (2014) 2421–2427.
[9] Z. Ma, D. Liu, Y. Zhu, Z. Li, Z. Li, H. Tian, H. Liu, Graphene oxide/chitin nanofibril composite foams as column adsorbents for aqueous pollutants, Carbohydr. Polym., 144 (2016) 230–237.
[10] H.S. Jamwal, S. Kumari, G.S. Chauhan, N.S. Reddy, J.-H. Ahn, Silica-polymer hybrid materials as methylene blue adsorbents, J. Environ. Chem. Eng., 5 (2017) 103–113.
[11] X. Liu, W. Gong, J. Luo, C. Zou, Y. Yang, S. Yang, Selective adsorption of cationic dyes from aqueous solution by polyoxometalate-based metal–organic framework composite, Appl. Clay Sci., 362 (2016) 517–524.
[12] Y.M. Zhou, S.Y. Fu, H. Liu, S.P. Yang, H.Y. Zhan, Removal of methylene blue dyes from wastewater using cellulose-based superadsorbent hydrogels, Polym. Eng. Sci., 51 (2011) 2417–2424.
[13] S. Xu, Y. Lv, X. Zeng, D. Cao, ZIF-derived nitrogen-doped porous carbons as highly efficient adsorbents for removal of organic compounds from wastewater, Chem. Eng. J., 323 (2017) 502–511.
[14] T. Yao, S. Guo, C.F. Zeng, C.Q. Wang, L.X. Zhang, Investigation on efficient adsorption of cationic dyes on porous magnetic polyacrylamide microspheres, J. Hazard. Mater., 292 (2015) 90–97.
[15] R. Hazzaa, M. Hussein, Adsorption of cationic dye from aqueous solution onto activated carbon prepared from olive stones, Environ. Technol. Innovation, 4 (2015) 36–51.
[16] A.A. Babaei, S.N. Alavi, M. Akbarifar, K. Ahmadi, A. Ramazanpour Esfahani, B. Kakavandi, Experimental and modeling study on adsorption of cationic methylene blue dye onto mesoporous biochars prepared from agrowaste, Desal. Wat. Treat., 57 (2016) 27199–27212.
[17] W. Wang, Y. Ma, A. Li, Q. Zhou, W. Zhou, J. Jin, Two novel multi-functional magnetic adsorbents for effective removal of hydrophilic and hydrophobic nitroaromatic compounds, J. Hazard. Mater., 294 (2015) 158–167.
[18] Y. Zhu, D. Jiang, D. Sun, Y. Yan, C. Li, Fabrication of magnetic imprinted sorbents prepared by Pickering emulsion polymerization for adsorption of erythromycin from aqueous solution, J. Environ. Chem. Eng., 4 (2016) 3570–3579.
[19] Y.F. Zhu, W.B. Wang, Y.A. Zheng, F. Wang, A.Q. Wang, Rapid enrichment of rare-earth metals by carboxymethyl cellulose-based open-cellular hydrogel adsorbent from HIPEs template, Carbohydr. Polym., 140 (2016) 51–58.
[20] Y.F. Zhu, H.F. Zhang, W.B. Wang, X.S. Ye, Z.J. Wu, A.Q. Wang, Fabrication of a magnetic porous hydrogel sphere for efficient enrichment of Rb^+ and Cs^+ from aqueous solution, Chem. Eng. Res. Des., 125 (2017) 214–225.
[21] A. Lotierzo, S.A.F. Bon, A mechanistic investigation of Pickering emulsion polymerization, Polym. Chem., 8 (2017) 5100–5111.
[22] A. Samanta, S. Takkar, R. Kulshreshtha, B. Nandan, R.K. Srivastava, Facile fabrication of composite electrospun nanofibrous matrices of poly(epsilon-caprolactone)-silica based Pickering emulsion, Langmuir, 33 (2017) 8062–8069.
[23] Y. Zhang, J. Wu, B. Wang, X. Sui, Y. Zhong, L. Zhang, Z. Mao, H. Xu, Cellulose nanofibril-reinforced biodegradable polymer composites obtained via a Pickering emulsion approach, Cellulose, 24 (2017) 3313–3322.
[24] M.S. Silverstein, Emulsion-templated polymers: contemporary contemplations, Polymer, 126 (2017) 261–282.
[25] Y.-W. Wang, C.-W. Chen, J.H. Hsieh, W.J. Tseng, Preparation of Ag/TiO_2 composite foams via Pickering emulsion for bactericide and photocatalysis, Ceram. Int., 43 (2017) S797–S801.
[26] E.H. Mert, H. Yıldırım, A.T. Üzümcü, H. Kavas, Synthesis and characterization of magnetic polyHIPEs with humic acid surface modified magnetic iron oxide nanoparticles, React. Funct. Polym., 73 (2013) 175–181.

[27] T.T. Lu, Y.F. Zhu, Y.X. Qi, W.B. Wang, A.Q. Wang, Magnetic chitosan–based adsorbent prepared via Pickering high internal phase emulsions for high-efficient removal of antibiotics, Int. J. Biol. Macromol., 106 (2018) 870–877.
[28] Y.A. Zheng, Y.T. Xie, A.Q. Wang, Rapid and wide pH-independent ammonium-nitrogen removal using a composite hydrogel with three-dimensional networks, Chem. Eng. J., 179 (2012) 90–98.
[29] A.M.K. Najjar, W.M.Z.W. Yunus, M.B. Ahmad, M.Z.A. Rahman, Preparation and characterization of poly(2-acrylamido-2-methylpropane-sulfonic acid) grafted chitosan using potassium persulfate as redox initiator, J. Appl. Polym. Sci., 77 (2000) 2314–2318.
[30] Y.F. Zhu, W.B. Wang, H.F. Zhang, X.S. Ye, Z.J. Wu, A.Q. Wang, Fast and high-capacity adsorption of Rb^+ and Cs^+ onto recyclable magnetic porous spheres, Chem. Eng. J., 327 (2017) 982–991.
[31] Y. Ho, A review of potentially low cost adsorbent for heavy metals, Scientometrics, 59 (2004) 171–177.
[32] Y. Ho, G. McKay, A comparison of chemisorption kinetic models applied to pollutant removal on various sorbents, Process Saf. Environ. Prot., 76 (1998) 332–340.
[33] S. Zhang, M. Zeng, J. Li, J. Li, J. Xu, X. Wang, Porous magnetic carbon sheets from biomass as an adsorbent for the fast removal of organic pollutants from aqueous solution, J. Mater. Chem. A, 2 (2014) 4391–4397.
[34] Y.F. Zhu, Y.A. Zheng, F. Wang, A.Q. Wang, Monolithic supermacroporous hydrogel prepared from high internal phase emulsions (HIPEs) for fast removal of Cu^{2+} and Pb^{2+}, Chem. Eng. J., 284 (2016) 422–430.
[35] S. Kuppusamy, K. Venkateswarlu, P. Thavamani, Y.B. Lee, R. Naidu, M. Megharaj, Quercus robur acorn peel as a novel coagulating adsorbent for cationic dye removal from aquatic ecosystems, Ecol. Eng., 101 (2017) 3–8.
[36] H. You, J. Chen, C. Yang, L. Xu, Selective removal of cationic dye from aqueous solution by low-cost adsorbent using phytic acid modified wheat straw, Colloids Surf., A, 509 (2016) 91–98.
[37] A.K. Hammed, N. Dewayanto, D. Du, M.H. Ab Rahim, M.R. Nordin, Novel modified ZSM-5 as an efficient adsorbent for methylene blue removal, J. Environ. Chem. Eng., 4 (2016) 2607–2616.
[38] L. Li, L. Chen, H. Shi, X. Chen, W. Lin, Evaluation of mesoporous bioactive glass (MBG) as adsorbent for removal of methylene blue (MB) from aqueous solution, J. Environ. Chem. Eng., 4 (2016) 1451–1459.
[39] L. Kong, F. Qiu, Z. Zhao, X. Zhang, T. Zhang, J. Pan, D. Yang, Removal of brilliant green from aqueous solutions based on polyurethane foam adsorbent modified with coal, J. Cleaner Prod., 137 (2016) 51–59.
[40] R. Kumar, M.O. Ansari, M. Barakat, Adsorption of brilliant green by surfactant doped polyaniline/MWCNTs composite: evaluation of the kinetic, thermodynamic, and isotherm, Ind. Eng. Chem. Res., 53 (2014) 7167–7175.
[41] R. Kumar, M. Barakat, Decolourization of hazardous brilliant green from aqueous solution using binary oxidized cactus fruit peel, Chem. Eng. J., 226 (2013) 377–383.
[42] R. Dutta, T.V. Nagarjuna, S.A. Mandavgane, J.D. Ekhe, Ultrafast removal of cationic dye using agrowaste-derived mesoporous adsorbent, Ind. Eng. Chem. Res., 53 (2014) 18558–18567.
[43] T.A. Khan, R. Rahman, E.A. Khan, Adsorption of malachite green and methyl orange onto waste tyre activated carbon using batch and fixed-bed techniques: isotherm and kinetics modeling, Model. Earth Syst. Environ., 1 (2017) 1–14.
[44] P. Sharma, B.K. Saikia, M.R. Das, Removal of methyl green dye molecule from aqueous system using reduced graphene oxide as an efficient adsorbent: kinetics, isotherm and thermodynamic parameters, Colloids Surf., A, 457 (2014) 125–133.
[45] T. Mekhalif, K. Guediri, A. Reffas, D. Chebli, A. Bouguettoucha, A. Amrane, Effect of acid and alkali treatments of a forest waste, *Pinus brutia* cones, on adsorption efficiency of methyl green, J. Dispersion Sci. Technol., 38 (2017) 463–471.
[46] M. Bahgat, A.A. Farghali, W. El Rouby, M. Khedr, M.Y. Mohassab-Ahmed, Adsorption of methyl green dye onto multi-walled carbon nanotubes decorated with Ni nanoferrite, Appl. Nanosci., 3 (2013) 251–261.
[47] I. Langmuir, The constitution and fundamental properties of solids and liquids, Part I. Solids, J. Am. Chem. Soc., 38 (1916) 2221–2295.
[48] H. Freundlich, Over the adsorption in solution, J. Phys. Chem., 57 (1906) 1100–1107.
[49] J. Gong, J. Liu, Z. Jiang, X. Wen, E. Mijowska, T. Tang, X. Chen, A facile approach to prepare porous cup-stacked carbon nanotube with high performance in adsorption of methylene blue, J. Colloid Interface Sci., 445 (2015) 195–204.
[50] M.P. Tavlieva, S.D. Genieva, V.G. Georgieva, L.T. Vlaev, Kinetic study of brilliant green adsorption from aqueous solution onto white rice husk ash, J. Colloid Interface Sci., 409 (2013) 112–122.

Supplementary information

The Fe_3O_4-MNPs prepared by hydrothermal method had the regular spherical structure and the diameter was about 110 nm (Fig. S1(a)), and it increased to 150 nm and had many protuberances in the surface after modification with organosilane (Fig. S2(a)). Additionally, the XRD patterns (Fig. S2(b)) of Fe_3O_4-MNPs-M suggested that the characteristic peaks of Fe_3O_4-MNPs had no significant changes but become shorter and wider, indicating that the crystalline structure of Fe_3O_4 did not change after surface modification.

The Fe_3O_4-MNPs and the Fe_3O_4-MNPs-M showed a broad band around 582 and 568 cm^{-1}, corresponding to the Fe–O vibration related to the magnetite phase. For the Fe_3O_4-MNPs-M, the absorption bands at 1,095 and 951 cm^{-1}

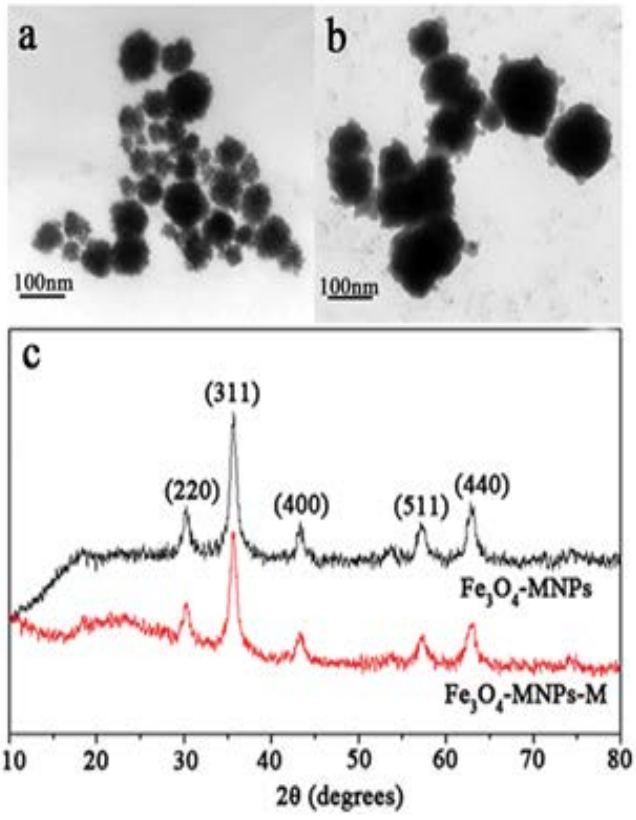

Fig. S1. TEM images of Fe_3O_4-MNPs (a) and Fe_3O_4-MNPs-M (b); XRD patterns of Fe_3O_4-MNPs and Fe_3O_4-MNPs-M.

corresponded to the asymmetric stretching and bending of silanol groups (Si–OH) on the Fe_3O_4-MNPs-M surface, respectively. A band at about 3,416 cm^{-1} corresponded to the overlapping of N–H and C–H vibration with siloxane and silanol groups, which was overlapped by the O–H stretching vibration. And the characteristic band appeared at 799 cm^{-1} was attributed to the symmetric stretching vibration of Si–O–Si. These results provide the evidences that the Fe_3O_4-MNPs have been modified successfully with APTMS.

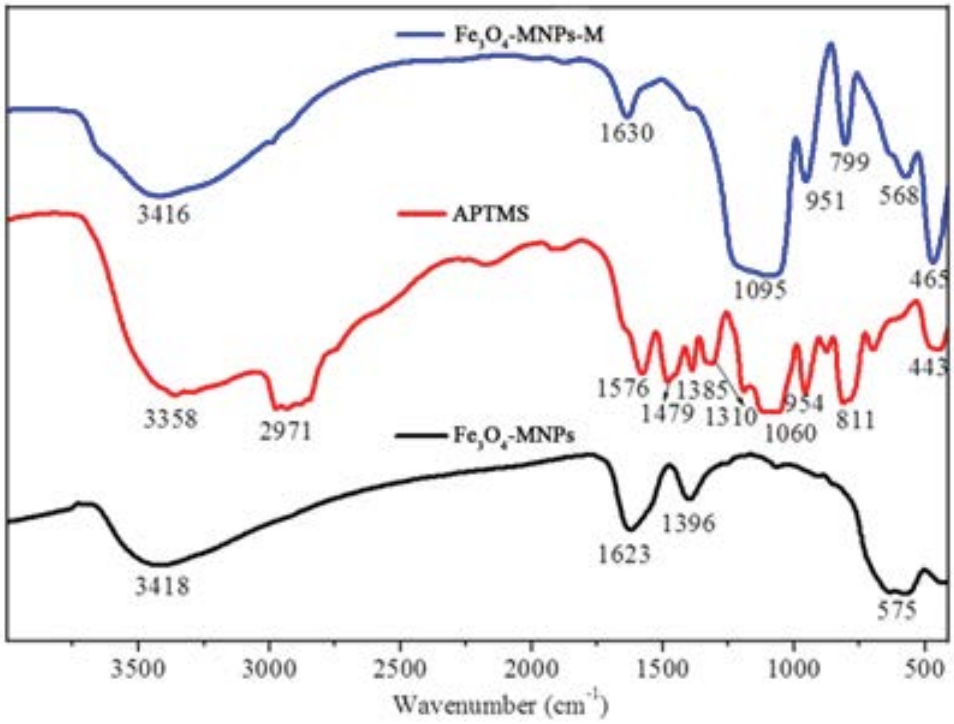

Fig. S2. FTIR spectra of Fe_3O_4-MNPs, APTMS, and Fe_3O_4-MNPs-M.

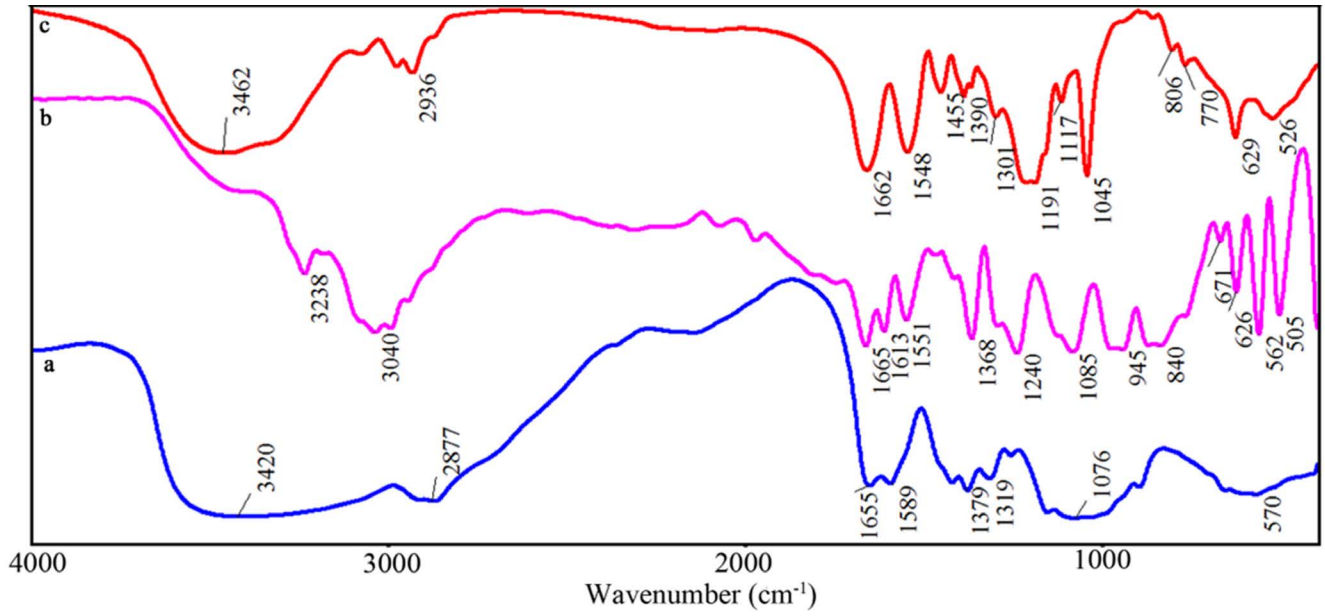

Fig. S3. The FTIR spectra of CTS (a), AMPS (b), and CTS-*g*-AMPS-2 (c).

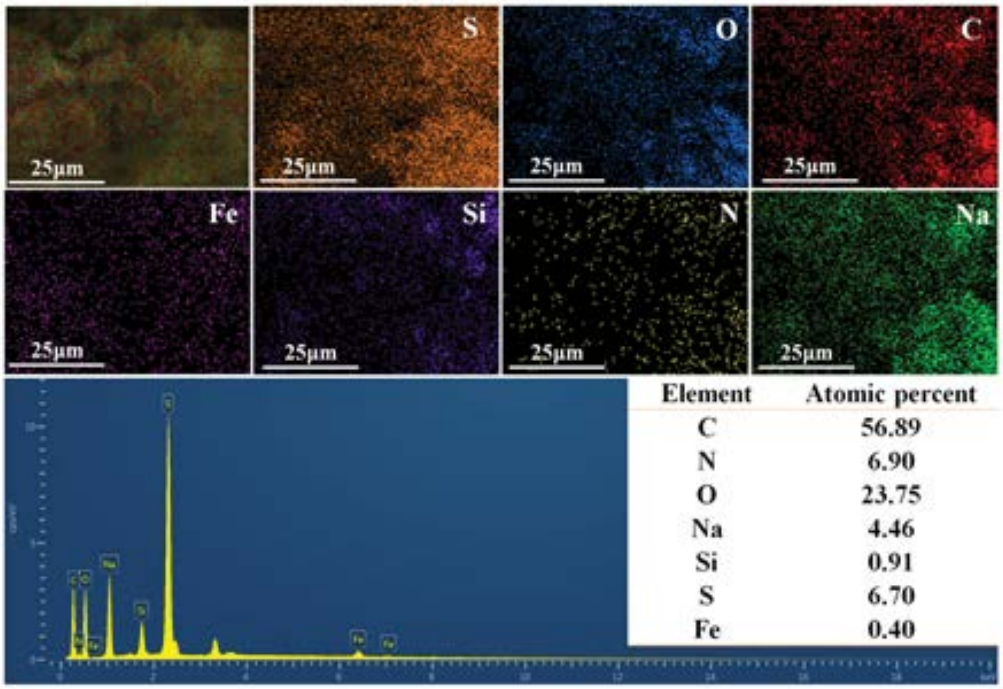

Element	Atomic percent
C	56.89
N	6.90
O	23.75
Na	4.46
Si	0.91
S	6.70
Fe	0.40

Fig. S4. EDX elemental mappings of S, O, C, Fe, Si, N, Na and EDX spectrum of magnetic porous adsorbent.

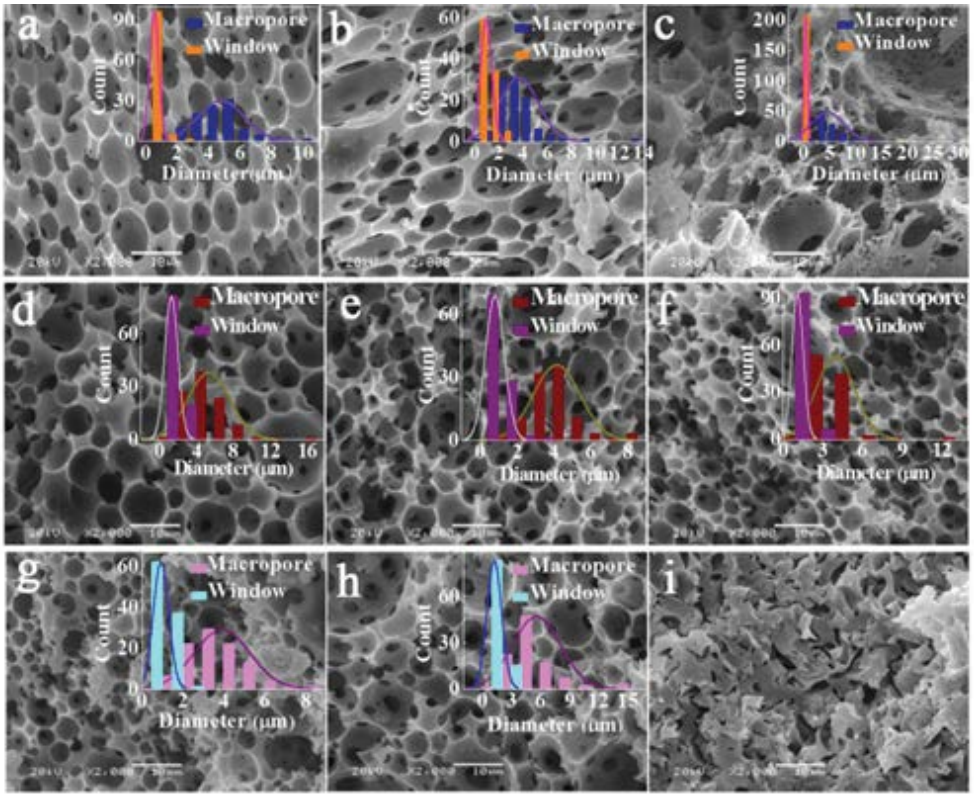

Fig. S5. SEM images and size distributions of the porous adsorbents prepared with different amounts of Fe_3O_4-MNPs-M (a) 0.5%, (b) 1.5%, and (c) 2%; Pluronic F68 (d) 1%, (e) 3%, and (f) 4%; and internal phase volume (g) 80%, (h) 85.7%, and (i) 88.9%. (a)–(h): macropore: 4.79, 3.65, 4.60, 5.42, 4.14, 3.97, 3.88, and 5.57 μm; window: 0.55, 0.95, 0.42, 1.35, 0.82, 1.11, 0.93, and 1.18 μm; the total drop surface area of adsorbents (*Sd*): 15.03, 19.72, 15.65, 13.28, 16.36, 18.13, 18.55, and 12.92 m^2. When the volume fractions of dispersed phase reached 88.9%, the pore size and total drop surface area of magnetic adsorbent could not be obtained, due to the pore shrinkage and collapse during drying.

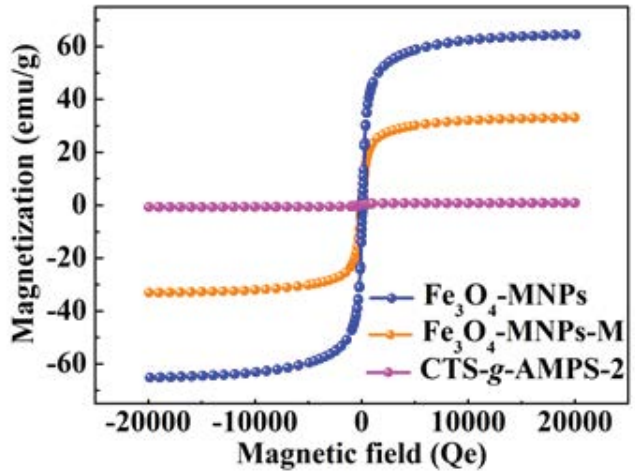

Fig. S6. The magnetic hysteresis loops of the Fe_3O_4-MNP, Fe_3O_4-MNPs-M, and CTS-*g*-AMPS-2 adsorbent.

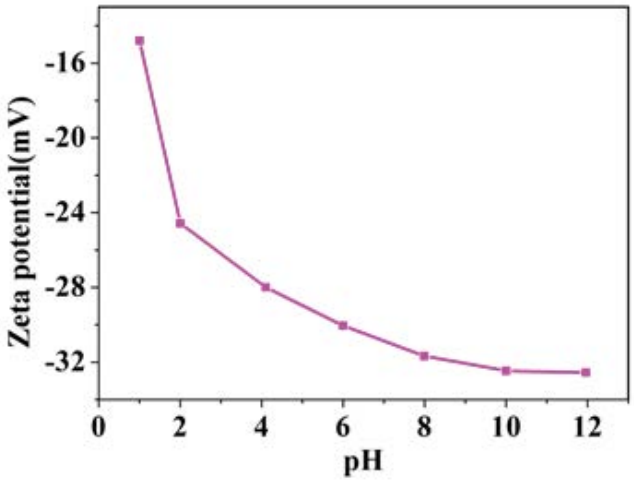

Fig. S7. The zeta potentials of the CTS-*g*-AMPS-2 in the pH range of 1.0–12.0.

Table S1
Composition of the Pickering-HIPEs

Adsorbents	Fe_3O_4-MNPs-M (%)	Pluronic F68 (%)	Internal phase volume (PX, %)
CTS-*g*-AMPS-1	0.5	2	75
CTS-*g*-AMPS-2	1	2	75
CTS-*g*-AMPS-3	1.5	2	75
CTS-*g*-AMPS-4	2	2	75
CTS-*g*-AMPS-5	1	1	75
CTS-*g*-AMPS-6	1	3	75
CTS-*g*-AMPS-7	1	4	75
CTS-*g*-AMPS-8	1	2	80
CTS-*g*-AMPS-9	1	2	85.7
CTS-*g*-AMPS-10	1	2	88.9

Table S2
The zeta potentials of the magnetic porous adsorbent

	Before the adsorption	After the adsorption		
		MB	BG	MG
Zeta (mV)	−23.5 mV	−1.26	−1.37	−1.34